Catalyzing overall water splitting at an ultralow cell voltage of 1.42 V via coupled Co-doped NiO nanosheets with carbon

Hongyuan Yang[a], Ziliang Chen[a], Weiju Hao[a], Hongbin Xu[a], Yanhui Guo[a,b], Renbing Wu[a,b,*]

[a] Department of Materials Science, Fudan University, Shanghai 200433, PR China
[b] Shanghai Innovation Institute for Materials, Shanghai 200444, PR China

ARTICLE INFO

Keywords:
Co-doped NiO
Coupled conductive carbon
Porous ultrathin nanosheets
Electrocatalysts
Overall water splitting

ABSTRACT

The development of nonprecious, highly active and robust bifunctional electrocatalysts for both hydrogen and oxygen evolution reactions via water splitting is of primary significance, but still remains challenging. Herein, we develop a three-dimension (3D) heterostructured catalyst ($Ni_{0.82}Co_{0.18}O@C/NF$) by coupling of ultrathin Co-doped NiO ($Ni_{0.82}Co_{0.18}O$) nanosheets and carbon on nickel foam (NF) with synergism of geometric engineering and electronic modulation. Benefiting from the unique 3D configuration, highly exposed active sites and the synergistic effect of the active $Ni_{0.82}Co_{0.18}O$ and the carbon, the catalyst exhibits exceptional hydrogen evolution reaction (HER) and oxygen evolution reaction (OER) performance with low overpotentials and Tafel slopes and excellent stability in alkaline media. Specifically, the $Ni_{0.82}Co_{0.18}O@C/NF$ employed as catalyst for both anode and cathode enables an alkaline electrolyzer to achieve a current density of $10\,mA\,cm^{-2}$ by a cell voltage of only 1.42 V, which is not only much lower than that of the integrated performance of the commercial noble Pt/C and IrO_2/C catalyst couple ($\sim 1.61\,V$), but also superior to most reported results to date. Our finding may provide a new opportunity to design advanced bifunctional catalysts toward practical overall water splitting.

1. Introduction

The rapidly ever-growing energy consumption and environmental problems have stimulated considerable attention in developing renewable and sustainable energy technologies [1–11]. Among various promising strategies, electrochemical water splitting consisting of hydrogen evolution reaction (HER) on the cathode and oxygen evolution reaction (OER) on the anode is regarded as one of the most sustainable solution to generate high-purity hydrogen on a large-scale and store energy from intermittently renewable sources [12–17]. Nevertheless, these two half reactions are both thermodynamic uphill and kinetically not favored, which normally require highly efficient catalyst to reduce the overpotential and promote the reaction process [18–23]. Currently, noble Pt-based materials are the most active HER catalysts, while Ir/Ru-based oxides are considered as the benchmark for OER catalysts. Unfortunately, the scarcity and high cost of these precious metals have seriously hampered the practical application in water splitting devices. As a result, it is of utmost urgency to develop low-cost and highly active catalyst based on earth abundant elements.

With respect to cost-effective, catalytic activity and long-term stability, transition metals or their derivatives such as chalcogenides, nitrides and phosphides have been widely investigated as HER catalyst [24–29], whereas perovskites and transition metal hydroxides/oxides have been intensively explored for the OER catalyst [30–33]. Although great progress that has been made in this area, very few of them are capable of catalyzing both HER and OER process effectively in an integrated water splitting cell, probably due to the fact that the activity and durability of these catalysts are mismatched in wide pH ranges [34]. Considering the facile applicability in implementing the overall water splitting system, developing a highly efficient bifunctional catalyst for achieving HER and OER simultaneously in the same electrolyte is highly desirable but still remains a grand challenge.

Recently, nickel-based compounds have been demonstrated as promising electrocatalysts to catalyze both HER and OER because of their earth abundance, environmental benignity and facile electronic structure regulation [35–38]. For example, Luo et al. reported that NiFe layered hydroxide (LDH) as bifunctional electrocatalyst could achieve $10\,mA\,cm^{-2}$ at a cell voltage of 1.7 V in an alkaline medium [35]. Jia et al. developed a bifunctional electrocatalyst consisting of Ni-Fe hydrooxide nanosheet and defective graphene and found it could deliver a current density of $20\,mA\,cm^{-2}$ at a cell voltage of 1.5 V [36]. Hu et al. prepared hierarchical Ni-Co-P hollow nanobrick, which is capable of delivering a cell voltage of 1.62 V at $10\,mA\,cm^{-2}$ for overall water splitting [37]. Although a series of nickel-based catalysts have been

---

designed to simultaneously catalyze both HER and OER, their performance is still unsatisfactory possibly due to the poor electrical conductivity and low surface active exposure, resulting in large cell voltages (over 1.5 V, determined at the current density of 10 mA cm^{-2}). To make water splitting economically viable and scalable, rational design of more efficient bifunctional catalysts that can achieve the overall water electrolysis at lower cell voltage is of great importance.

Nanostructure engineering and electronic regulation are considered as effective approaches to optimize the activity of electrocatalysts [39–48]. Particularly, delicate engineering of transition metal-based materials from bulk to ultrathin nanosheets with porous structure not only increases the accessible surface area but also provides abundant active edges and expose more low coordinated surface atoms, thus leading to enhanced catalytic activity [49]. On the other hand, the electronic regulation through heteroatoms doping, defect/interface tailoring and hybridization with conductive carbonaceous has also been proven to be beneficial to the catalytic performance. For instance, our previous work showed that the OER activity of cobalt sulfide/carbon composite catalyst could be improved by optimizing the electronic coupling between the components [21]. Trotochaud et al. demonstrated that Fe-doping could greatly improve the electrical conductivity and modify the electronic structure of NiOOH, enabling Ni-Fe oxyhydroxide promising OER catalyst [50]. Liu et al. reported that the electronic structure of NiS_2 could be modulated from semiconductive characteristics to metallic features via heteroatom defect, exhibiting enhanced catalytic activity towards the overall water splitting [51]. Inspired by the above points, it can be expected that the integration of two-dimensional (2D) porous nickel-based nanosheets with rich defects, appropriate heteroatoms doping together with the coupled conductive carbon may substantially promote the catalytic performance.

Herein, we have developed a hybrid catalyst consist of Co-doped NiO ($Ni_{0.82}Co_{0.18}O$) and strongly coupled carbon directly grown on nickel foam (NF) by an immersion-adsorption-pyrolysis strategy, representing as a highly efficient bifunctional electrocatalyst for overall water splitting. The as-synthesized hybrid $Ni_{0.82}Co_{0.18}O@C/NF$ catalyst can be directly used in an alkaline electrolyzer and avoids the use of any undesired polymeric binders or conducting agent, which exhibits outstanding catalytic activity and stability toward both HER and OER. Remarkably, the $Ni_{0.82}Co_{0.18}O@C/NF$ catalyst served as both the anode and cathode for overall water splitting enabled an alkaline electrolyzer with ~10 mA cm^{-2} at a cell voltage of only 1.42 V, which outperformed most bifunctional electrocatalysts.

2. Experimental section

2.1. Synthesis of NiCo-LDH/NF

A piece of nickel foam (NF, 2 cm × 3 cm) was washed by deionized water, acetone, ethanol in the order and dried in the vacuum. Next, the cleaned NF was immersed in a mixture solution of ethanol (150 mL) and deionized water (50 mL) containing 75 mM Co(NO$_3$)$_2$·6H$_2$O, 150 mM Ni(NO$_3$)$_2$·6H$_2$O and 170 mM $C_6H_{12}N_4$ at a constant temperature of 90 °C for 9 h. Afterwards, the NiCo-LDH/NF was washed by deionized water and dried in air.

2.2. Synthesis of NiCo-LDH@PDA/NF

40 mg dopamine was dissolved in 60 mL Tris-Buffer solution whose pH value was 8.5. The as-prepared NiCo-LDH/NF was immersed in the solution to be coated with polydopamine (PDA) for 24 h and noted as NiCo-LDH@PDA. Tris-Buffer solution was prepared by dissolving 0.3028 g of Tris-based solution in 250 mL of deionized water. Noted that NiCo-LDH/NF coated with PDA for 12 and 36 h were denoted as NiCo-LDH@PDA-12 h and NiCo-LDH@PDA-36 h, respectively.

2.3. Synthesis of Ni$_{0.82}$Co$_{0.18}$O@C/NF

The dried NiCo-LDH@DPA was heated to 500 °C under nitrogen atmosphere for 2 h and allowed to cool to room temperature. Noted that the products obtained using NiCo-LDH@PDA-12 h and NiCo-LDH@PDA-36 h were named as $Ni_{0.82}Co_{0.18}O@C/NF$-12 h and $Ni_{0.82}Co_{0.18}O@C/NF$-36 h, while $Ni_{0.82}Co_{0.18}O/NF$ was synthesized without coating with dopamine.

2.4. Synthesis of NiO@C/NF, Ni$_{0.88}$Co$_{0.12}$O@C/NF and Ni$_{0.73}$Co$_{0.27}$O@C/NF

The synthetic process of NiO@C/NF, $Ni_{0.88}Co_{0.12}O@C/NF$ and $Ni_{0.73}Co_{0.27}O@C/NF$ was similar to that of $Ni_{0.82}Co_{0.18}O@C/NF$ except that NiO@C/NF was synthesized without the additional of Co(NO$_3$)$_2$·6H$_2$O, while $Ni_{0.88}Co_{0.12}O@C/NF$ and $Ni_{0.73}Co_{0.27}O@C/NF$ were sythesized with a Ni/Co ratio of 5:1 and 1:2, respectively.

2.5. Materials characterization

The morphology and microstructure of the products were characterized by field-emission scanning electron microscope (FESEM, JEOL JSM-6700 F) and transmission electron microscope (TEM, JEOL JEM-2100 F). Powder X-ray diffraction (XRD) characterizations were operated on a D8 ADVANCE X-ray diffractometer with Cu Kα radiation. The amounts of element Ni and Co were determined through an inductively coupled plasma-atomic emission spectrometer (ICP-AES, USA VARIAN). Atomic force microscopy (AFM) were taken on the Bruker Edge Dimension with ScanAsyst. X-ray photoelectron spectroscopy (XPS) was performed on a Kratos XSAM-800 spectrometer equipped with an Mg Kα radiation source. Raman spectra were collected from Confocal microscope Raman spectrometer system (Witec Alpha 300).

2.6. Electrochemical measurements

The electrochemical measurements were performed on an Autolab (PGSTAT302 N) electrochemical workstation in a three-electrode cell at room temperature. The linear sweep voltammetry (LSV) was conducted in 1.0 M KOH solution using a saturated calomel electrode (SCE) and a graphite rod as the reference and the counter electrode, respectively. The 3D $Ni_{0.82}Co_{0.18}O@C$ supported on NF (0.5 cm^{-2}) was used as the working electrode directly. The SCE electrode was calibrated with respect to reversible hydrogen electrode (RHE) in a three-electrode system under around 25 °C, in which Pt wire, SCE and Pt plate were applied as working, reference and counter electrode, respectively. After 1 M KOH was highly saturated with pure hydrogen, CVs were recorded at a scan rate of 1 mV s^{-1}. The average of two potentials at which the zero-current-crossing points was taken to be the thermodynamic potential for hydrogen electrode reactions (1.059 V, Fig. S1) [52]. All potentials were normalized to reversible hydrogen electrode (RHE) according to the equation: $E_{vs.RHE} = E_{vs.SCE} + 1.059\,V + 95\%\,IR$. The overall water splitting was conducted in two-electrode system, where the catalyst was used as both the cathode and anode. For comparison, the Pt/C/NF as the cathode and IrO$_2$/NF as the anode were also evaluated. For the preparation of Pt/C/NF or IrO$_2$/NF electrode, 4 mg Pt/C or IrO$_2$ powder and 30 μL nafion solution were mixed in 970 μL ethanol solution, follwed by sonicated for 30 min to obtain a homogenous suspension, which was then dropped onto the surface of bare NF for several times [53].

The Faradaic efficiency (FE) was defined by the ratio of molar amounts of the generated O$_2$ or H$_2$ to the those of theoretical one. The experimental molar amount of gas can be calculated by the equation: $N_{ex} = V/V_m$, where V is volume of the measured gas and V_m (24.5 L mol^{-1}, RT) is the molar volume. O$_2$ evolution was measured using a fluorescence-based oxygen sensor under a constant potential and the volume of H$_2$ was determined by water drainage method [54,55]. The
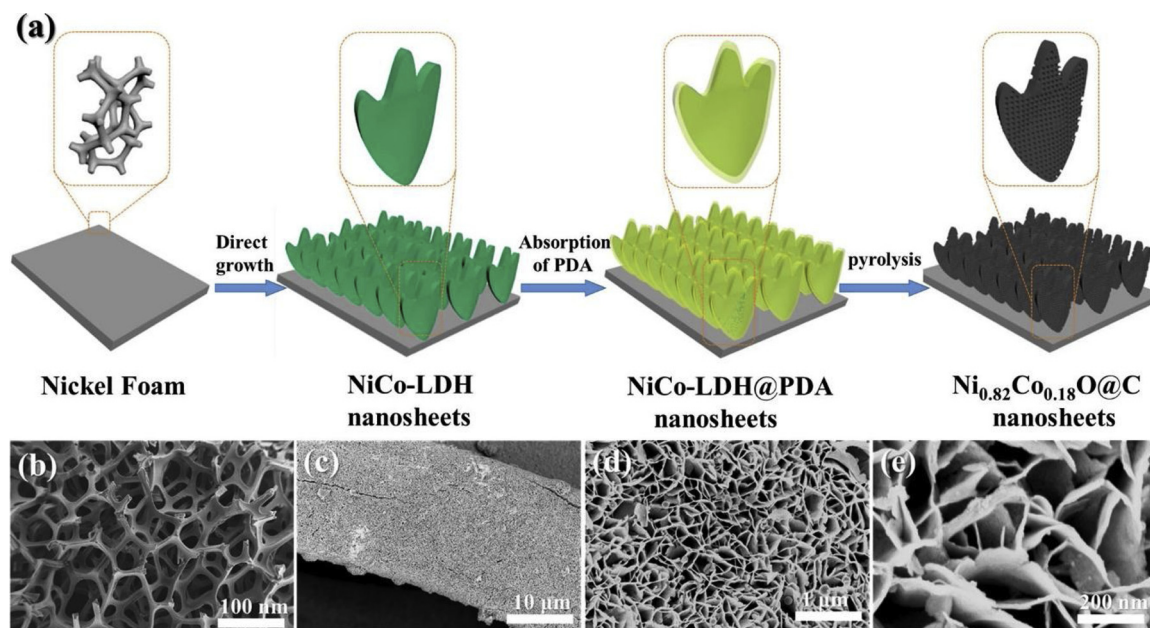
Fig. 1. (a) The schematic illustration of the synthetic process for the $Ni_{0.82}Co_{0.18}O@C$ nanosheets arrays grown on the Ni foam substrate, (b) FESEM image of Ni foam and (c–e) FESEM images of $Ni_{0.82}Co_{0.18}O@C/NF$.

theoretical molar quantity of O_2 or H_2 was calculated according to the Faraday law, $N_{th} = Q/(n*F)$, where Q (C) is total amount of electrical charge, F is Faradaic constant (96485.3 C mol^{-1}) and n is 4 for O_2 and 2 for H_2. The resulting FE was obtained by the ratio of N_{ex} to N_{th}. The stability evaluation was tested at 10 mA cm^{-2} for HER and overall water splitting while at 50 mA cm^{-2} for OER. The electrochemical impedance spectroscopy (EIS) curves were recorded at a current density 10 mA cm^{-2} within the frequency range from 10^{-2} to 10^5 Hz in 1.0 M KOH. The electrochemical double-layer capacitance (C_{dl}) which is proportional to electrochemically active surface areas (ECSA) were estimated by cyclic voltammetry (CV).

3. Results and discussion

The fabrication process of electrode is illustrated in Fig. 1a, which involves the direct growth of NiCo-layered double hydroxide (NiCo-LDH) nanosheet arrays on surface of NFs, adsorption of polydopamine (NiCo-LDH@PDA) followed by the subsequent pyrolysis treatment under a N_2 atmosphere to construct 3D porous $Ni_{0.82}Co_{0.18}O@C/NF$. The NF was selected as a binder-free substrate for the integrated electrode due to its 3D macroporous structure, excellent mechanical strength and electrical conductivity (Fig. 1b). Fig. S2a shows the X-ray diffraction (XRD) patterns of NiCo-LDH/NF, from which the peaks centered at 19.3°, 32.4°, 33° and 59.5° can be indexed to (001), (100), (100) and (003) planes of $Ni(OH)_2$ (JCPDS card# 14-0117) and Co $(OH)_2$ (JCPDS card# 30-0443) [56]. Field emission scanning electron microscopy (FESEM) image in Fig. S2b indicates that NiCo-LDH nanosheets were uniformly grown on the surface of NF after an immersion reaction. Fig. S3 shows the morphology of NiCo-LDH@PDA nanosheets, which was almost no change after the adsorption polydopamine. Fig. 1c − e present FESEM images of the resulting products, demonstrating that they inherit well the uniform distribution and sheet-like morphology of NiCo-LDH@PDA. Magnified FESEM image in Fig. 1e further reveals that the surface of products is rough, indicating the generation of porous structure during the pyrolysis process.

The XRD pattern of the as-synthesized $Ni_{0.82}Co_{0.18}O@C/NF$ is shown in Fig. 2a, together with the NiO@C/NF and bare NF as references. Compared with the XRD pattern of bare NF, in addition to the diffraction peaks belonged to the metallic Ni phase (JCPDS 65–2865), the diffraction peaks positioned at 37.1, 43.1 and 62.6° in the XRD

pattern of NiO@C/NF can be identified and correspond well to the (111), (200) and (220) planes of NiO, respectively (JCPDS card# 01-089 − 7130). By further comparing the XRD pattern of $Ni_{0.82}Co_{0.18}O@C/NF$ with that of NiO@C/NF, it can be known that although these two XRD patterns are quite similar in terms of the diffraction peaks shapes, the diffraction peaks positions of $Ni_{0.82}Co_{0.18}O@C/NF$ shifted to a lower angle direction as compared to those of NiO@C/NF, illustrating the increased lattice parameter in Co-doped sample, which should be due to the doping of Co into the NiO host lattice. Inductively coupled plasma atomic emission spectroscopy (ICP-AES) results revealed that the atomic ratio of Ni/Co is close to 0.82: 0.18 (Table S1), thus giving a stoichiometric formula of $Ni_{0.82}Co_{0.18}O$. The atomic force microscopy (AFM) image in Fig. 2b shows that the as-synthesized $Ni_{0.82}Co_{0.18}O@C$ nanosheets have a highly rough surface and irregular pores. The nanosheets exhibit a lateral size of ˜250 nm and a thickness of ∼3.3 nm (Fig. 2c).

X-ray photoelectron spectroscopy (XPS) measurements were further conducted to investigate the valence state of the elements. The XPS survey spectra shown in Fig. S4 revealed that the existence of Ni, Co, O and C elements in the surface of $Ni_{0.82}Co_{0.18}O@C$ nanosheets. High-resolution XPS spectrum of Ni 2p in Fig. 2d shows that two fitted spin-orbit doublets located at around 854.4 and 872.1 eV can be assigned to Ni $2p_{3/2}$ and $2p_{1/2}$ signals of Ni^{2+}, respectively. The peaks centered at 861 eV and 878.9 eV can be ascribed to the corresponding two satellite peaks of Ni^{2+} [57]. Meanwhile, the high-resolution XPS spectrum of Co 2p (Fig. 2e) can be deconvoluted into Co^{2+} $2p_{3/2}$ at 780.7 eV and Co^{2+} $2p_{1/2}$ at 795.9 eV along with their shake up satellites, without the observation of other valent states for Co specie [58]. These findings confirmed the doping of Co into NiO host lattice for the $Ni_{0.82}Co_{0.18}O@C$, consistent with the XRD results. In the fine-scanned O 1 s core level spectra (Fig. 2f), the binding energy at 529.6, 531.4, and 533.1 eV could be related to metal-oxygen bonds, low-coordinated oxygen ions at the surface/defect sites, and hydroxyl species of surface-adsorbed water molecules, respectively. The existence of low-co-ordinated oxygen ions at the surface/defect sites may provide rich active sites for water splitting [59,60]. Additionally, the carbon structure in the $Ni_{0.82}Co_{0.18}O@C$ composites was further characterized by Raman spectrum. As shown in Fig. S5, two peaks located at 1340 and 1588 cm^{-1} were observed, corresponding to D-band and G-bands of carbon, respectively, revealing the formation of carbon derived from
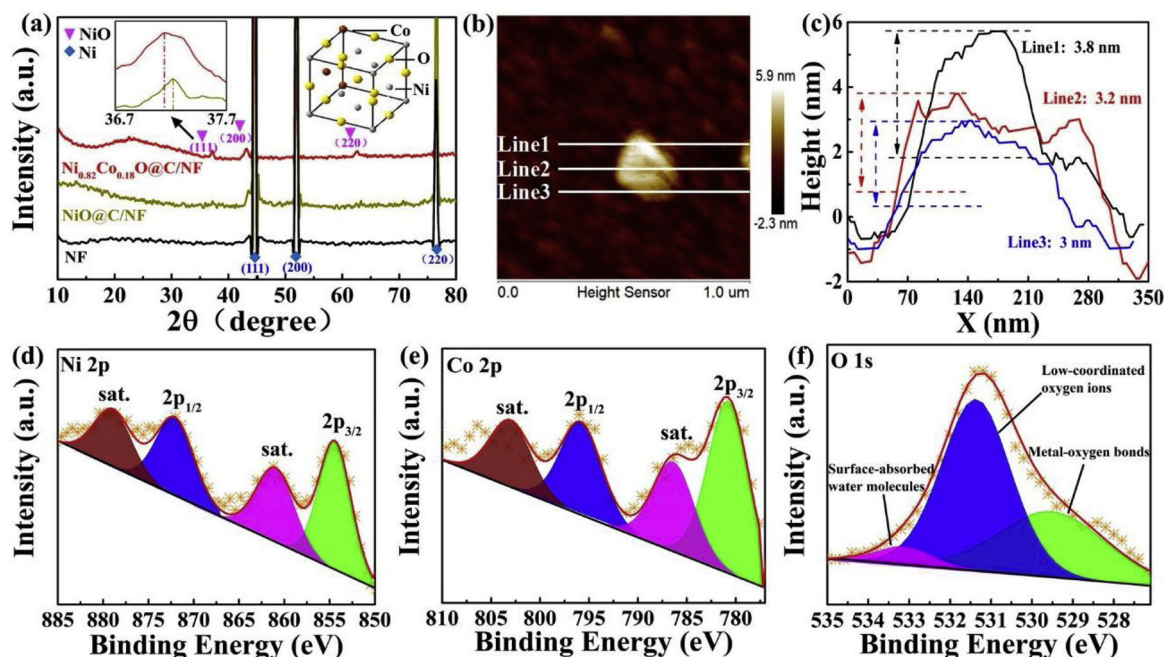
Fig. 2. (a) XRD patterns of $Ni_{0.82}Co_{0.18}O@C/NF$, $NiO@C/NF$ and bare NF (inset: zoomed-in view of XRD patterns and illustrated crystal structure); (b) AFM images of $Ni_{0.82}Co_{0.18}O@C$ nanosheet; (c) the corresponding line-scan profiles of $Ni_{0.82}Co_{0.18}O@C$ nanosheets with ~3.3 nm thickness; (d) Ni 2p XPS; (e) Co 2p XPS; and (f) O 1 s XPS spectra of $Ni_{0.82}Co_{0.18}O@C/NF$.

dopamine. The ratio of intensities of D-band and G-bands (I_D/I_G) is usually used to estimate the degree of defects in the carbon material, *i.e.* the larger the value of I_D/I_G, the more defects there are [61]. The calculated I_D/I_G for the $Ni_{0.82}Co_{0.18}O@C$ is 0.98, implying a large number of defects on the surface of carbon, which may be beneficial to the exposure of active sites.

The detailed microstructure of $Ni_{0.82}Co_{0.18}O@C$ was further examined by transmission electron microscope (TEM). In agreement with the FESEM findings, porous sheet-like structure can be observed in

Fig. 3a. High-resolution TEM image in Fig. 3b shows that the $Ni_{0.82}Co_{0.18}O$ crystallite is surrounded by amorphous carbon shell (marked with red dot line). A clear lattice fringes with an interplanar spacing of 0.21 nm can be indexed to the (200) plane of $Ni_{0.82}Co_{0.18}O$. Energy dispersive X-ray spectroscopy (EDS) elemental mapping of $Ni_{0.82}Co_{0.18}O@C$ indicates that the coexistence and the homogenous dispersion of Ni, Co, O and C elements within the nanosheets arrays (Fig. 3g–f).

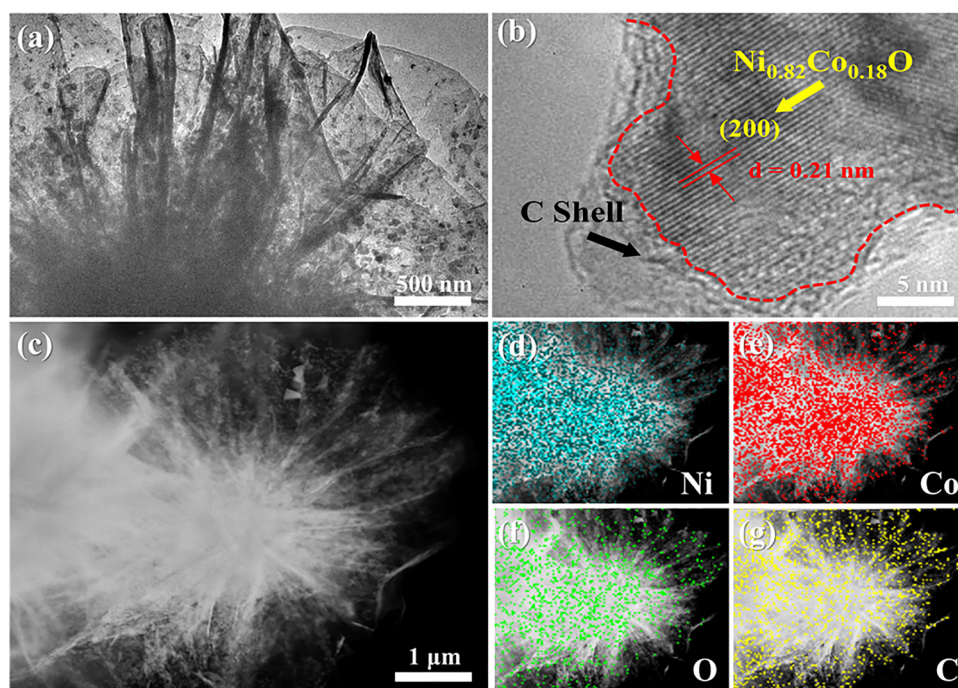The electrocatalytic HER performance of the $Ni_{0.82}Co_{0.18}O@C/NF$

Fig. 3. (a) TEM image and (b) HRTEM image of the $Ni_{0.82}Co_{0.18}O@C$ nanosheets, (c–g) the corresponding EDX elemental mapping images of $Ni_{0.82}Co_{0.18}O@C$ nanosheet.
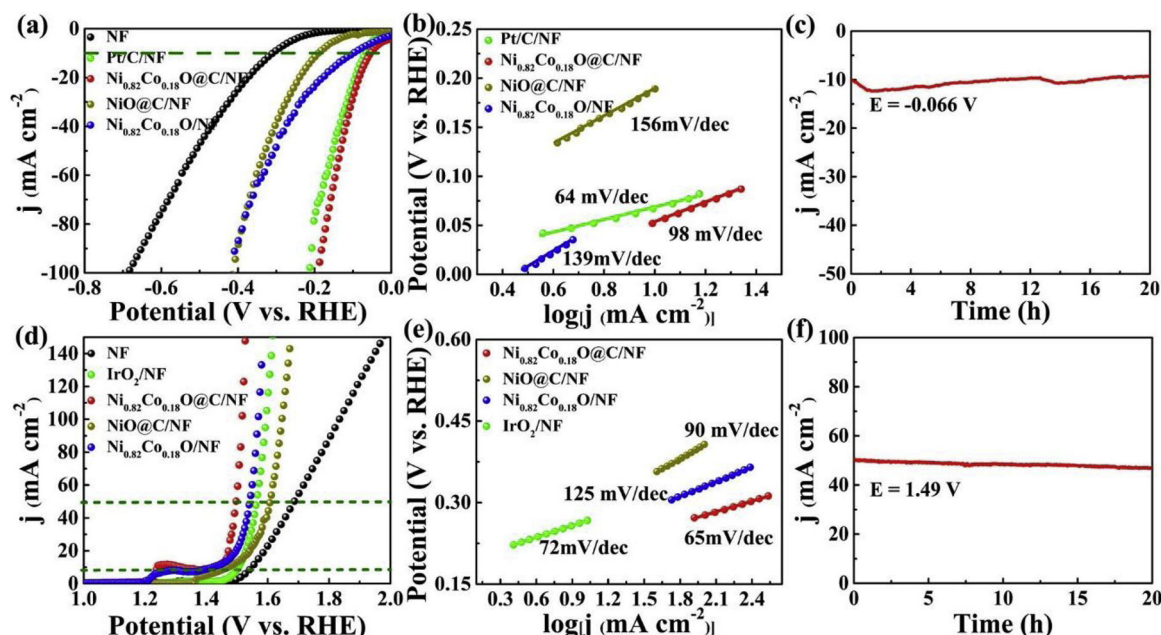
Fig. 4. (a) LSV polarization curves (at a scan rate of 5 mV s^{-1} with a 95% *IR* compensation) of bare NF, Pt/C/NF, $Ni_{0.82}Co_{0.18}O@C/NF$, NiO@C/NF and $Ni_{0.82}Co_{0.18}O/NF$ for HER; (b) corresponding Tafel plots of Pt/C/NF, $Ni_{0.82}Co_{0.18}O@C/NF$, NiO@C/NF and $Ni_{0.82}Co_{0.18}O/NF$; (c) I-t curve of $Ni_{0.82}Co_{0.18}O@C/NF$ for 20 h at a constant potential of –0.066 V (vs. RHE) during HER test; (d) LSV polarization curves of bare NF, IrO$_2$/NF, $Ni_{0.82}Co_{0.18}O@C/NF$, NiO@C/NF and $Ni_{0.82}Co_{0.18}O/NF$ for OER; (e) corresponding Tafel plots; (f) I-t curve of $Ni_{0.82}Co_{0.18}O@C/NF$ for 20 h at a constant potential of 1.49 V (vs. RHE) during OER test.

was evaluated in 1.0 M KOH by a standard three-electrode system. For comparison, NiO@C/NF, $Ni_{0.82}Co_{0.18}O/NF$, commercial Pt/C deposited on NF (Pt/C/NF) and bare NF were also investigated at the same experimental conditions. The linear sweep voltammetry (LSV) curves in Fig. 4a show that $Ni_{0.82}Co_{0.18}O@C/NF$ can afford a current density of 10 mA cm^{-2} at an overpotential of only 62 mV, which is not only much lower than the 102 mV for $Ni_{0.82}Co_{0.18}O/NF$, 155 mV for NiO@C/NF, 257 mV for bare NF, but also superior to the 80 mV for Pt/C/NF. Such performance also outperforms most of the transition metal-based electrocatalysts reported to date (Table S2). The excellent HER activity of the $Ni_{0.82}Co_{0.18}O@C/NF$ is further confirmed by the smallest Tafel slope of 98 mV/dec, compared with 139 mV/dec for the NiO@C/NF and 156 mV/dec for the $Ni_{0.82}Co_{0.18}O/NF$ (Fig. 4b). Electrochemical impedance spectroscopy (EIS) measurements were also conducted to explore the HER kinetics. As shown in Fig. S6, the fitted Nyquist impedance plot and equivalent circuit scheme exhibited an obvious decrease of the charge-transfer resistance (R_{ct}) from NiO@C/NF to $Ni_{0.82}Co_{0.18}O@C/NF$ (12.28 Ω for NiO@C/NF, 1.081 Ω for $Ni_{0.82}Co_{0.18}O/NF$ and 7.62 Ω for $Ni_{0.82}Co_{0.18}O@C/NF$), indicating a favorable reaction kinetics on the $Ni_{0.82}Co_{0.18}O@C/NF$. The corresponding EIS results and their parameters errors were also displayed in Table S3 [62,63]. In addition, a chronoamperometry was also performed to investigate the stability of $Ni_{0.82}Co_{0.18}O@C/NF$ electrode. As shown in Fig. 4c, the HER current density of $Ni_{0.82}Co_{0.18}O@C/NF$ exhibits no evident degradation over a prolonged HER test of 20 h at a constant potential of –0.066 V, indicating its good durability over the long-term electrolysis, which was further confirmed by a test under high current density of 100 mA cm^{-2} (Fig. S7). The electrochemical double-layer capacitance (C_{dl}) was also performed to estimate the electrochemical active surface areas (ECSA). The C_{dl} of $Ni_{0.82}Co_{0.18}O@C/NF$ (160 mF cm^{-2}) is higher than those of $Ni_{0.82}Co_{0.18}O/NF$ (130 mF cm^{-2}), NiO@C/NF (78 mF cm^{-2}) and bare NF (26 mF cm^{-2}), suggesting that the combination of Co-doped NiO with amorphous carbon is beneficial to the exposure of effective active sites, thus leading to much enhanced activity (Fig. S8).

We then assessed the OER catalytic activity of $Ni_{0.82}Co_{0.18}O@C/NF$, $Ni_{0.82}Co_{0.18}O/NF$, NiO@C/NF, commercial IrO$_2$ deposited on NF (IrO$_2$/

NF) and bare NF in 1.0 M KOH electrolyte. $Ni_{0.82}Co_{0.18}O@C/NF$ requires 320 mV to afford current density of 50 mA cm^{-2}, smaller than those of $Ni_{0.82}Co_{0.18}O/NF$ (372 mV), NiO@C/NF (440 mV), bare NF (516 mV) and 70 mV smaller than that of the state-of-the-art IrO$_2$/NF (Fig. 4d). Noted that it is not easy to accurately identify OER overpotential to achieve 10 mA cm^{-2} according to the LSV curve due to a redox process at low current densities. Table S3 gives the detailed comparison of OER performance for $Ni_{0.82}Co_{0.18}O@C/NF$ with other transition metal-based electrocatalysts, further highlighting its high OER activity. The OER kinetics on all electrodes can be illustrated by the Tafel plots (Fig. 4d). The $Ni_{0.82}Co_{0.18}O@C/NF$ electrode exhibits the lowest Tafel slopes of 65 mV/dec when compared with those of $Ni_{0.82}Co_{0.18}O/NF$ (90 mV/dec) and NiO@C/NF (125 mV/dec), implying a faster OER kinetic for $Ni_{0.82}Co_{0.18}O@C/NF$. Such fast process could also be demonstrated by the fitted EIS plot (Fig. S9), from which the $Ni_{0.82}Co_{0.18}O@C/NF$ possesses the smallest semicircle among all the samples. The related EIS parameters of R_{ct}, internal resistance (R_s) and other data can be observed in Table S5, in which $Ni_{0.82}Co_{0.18}O@C/NF$ had the lowest R_{ct} value, meaning its rapid charge transfer kinetics. To evaluate the stability of $Ni_{0.82}Co_{0.18}O@C/NF$ electrode for the OER, a continuous 20 h chronoamperometry measurement was carried out at a constant potential of 1.49 V and around 5% degradation was observed (Fig. 4f). Furthermore, when under a constant potential 1.52 V, this catalyst can maintain 100 mA cm^{-2} for 20 h (Fig. S10).

To investigate the effect of electronic modulation on the catalytic activity, NiO@C/NF with different Co contents were prepared (Table S1). As shown in high-resolution XPS spectra of samples (Fig. S11), with the increasing of the doped Co content, the binding energies of Ni 2p exhibited no change while those of Co 2p negatively shifted, indicating that the electrons might be promoted to transfer from Ni to Co atoms [51,64]. The catalytic activities of these samples and NiO@C/NF were also examined. Compared with $Ni_{0.88}Co_{0.12}O@C/NF$, $Ni_{0.73}Co_{0.27}O@C/NF$ and NiO@C/NF, $Ni_{0.88}Co_{0.12}O@C/NF$ exhibited the lowest overpotential for both HER and OER. Furthermore, the influence of the amorphous carbon on the electrochemical performance was also studied. The longer the polymerization time, the thicker the PDA thickness, leading to amorphous carbon shell with different thickness [65].
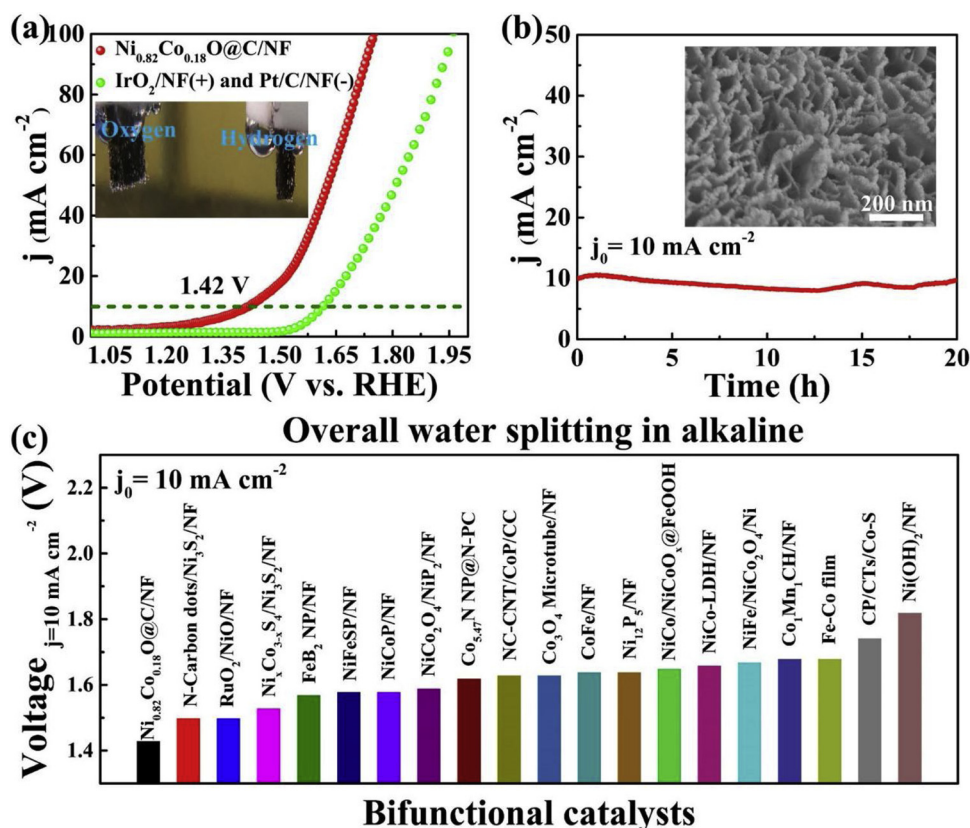
Fig. 5. (a) LSV curves (at a scan rate of 5 mV s^{-1} with a 95% *IR* compensation) of the typical two-electrode system by using $Ni_{0.82}Co_{0.18}O@C/NF$ as both cathode and anode in 1 M KOH, and NF supported $IrO_2||Pt/C$ for comparison (inset: an optical photo showing the generation of gas bubbles from the electrodes); (b) I-t curve for 20 h at a constant potential of 1.42 V during overall water splitting test (inset: FESEM image of the $Ni_{0.82}Co_{0.18}O@C/NF$ after long-term cycling test); (c) Comparison of the cell voltages to achieve a current density of 10 mA cm^{-2} for the $Ni_{0.82}Co_{0.18}O@C/NF$ catalyst with other latest bifunctional catalysts.

As shown in Fig. S13, $Ni_{0.82}Co_{0.18}O@C/NF$ obtained with a 24 h dopamine reaction still exhibited the best catalytic activity for both HER and OER among the investigated samples.

Given the outstanding bifunctional catalytic activity, a two-electrode system electrolyzer in which $Ni_{0.82}Co_{0.18}O@C/NF$ was utilized as both the cathode and anode was assembled to investigate the catalytic performance in practical applications. The catalytic performance of $IrO_2/NF||Pt/C/NF$ was also tested for comparison. As shown in Fig. 5a, the assembled electrolyzer can achieve the current density of 10 mA cm^{-2} at a low cell voltage of only 1.42 V, which is substantially lower than that of the coupled $IrO_2/NF||Pt/C/NF$ catalyst (1.61 V). The inset of Fig. 5a shows an optical photo of the overall water splitting cell, where the appreciable evolution of gas bubbles on the surface of both electrodes can be clearly observed. The Faradaic efficiency (FE) was further determined by dividing the measured amount of hydrogen and oxygen with the theoretic one during the chronoamperometry reaction. As shown in Fig. S14, both reactions exhibit outstanding FE which is about 99%, and the value ratio of H_2 and O_2 is 2:1. Remarkably, our $Ni_{0.82}Co_{0.18}O@C/NF$ catalyst has exceeded most state-of-the-art transition metal-based catalyst for overall alkaline water splitting as far as we know (Fig. 5c and Table S4). In addition, this two-electrode electrolyzer is stable over 20 h with the current loss of only 2.8% and 8% at a current density of 10 and 100 mA cm^{-2} (under a constant potential of 1.42 and 1.75 V), respectively, demonstrating the excellent long-term stability during the overall water splitting (Figs. 5b and S15). The morphology of the cycled $Ni_{0.82}Co_{0.18}O@C/NF$ catalyst is shown in the inset of Fig. 5b, from which a porous ultrathin nanosheet structure is still preserved. The surface chemical state of cathode catalyst was also characterized after cycling test and almost no changes were found in the XPS spectra (Fig. S16). The XPS spectra of the anode catalyst was shown in Fig. S17, in which the high-resolution Ni $2p_{3/2}$ was deconvoluted into two sub-peaks at 853.7 and 855.1 eV, identified as characteristic of Ni^{3+} and Ni^{2+}, respectively [57,66]. Notably, the Co $2p_{3/2}$ was also fitted well into two peaks centered at 778.8 and 780.2 eV,

indicating the partial oxidation during the OER process [67,68].

The superior performance of the $Ni_{0.82}Co_{0.18}O@C/NF$ catalyst toward overall water splitting can be mainly attributed to the following reasons. i) The appropriate incorporation of Co into NiO together with the coupled conductive carbon to form a hybrid composite with strongly interacting $Ni_{0.82}Co_{0.18}O$ and carbon species could not only improve its conductivity and charge transfer capability but also give rise to additional defect active sites and thus intrinsically high activity. ii) The porous ultrathin nanosheet arrays directly grown on nickel foam can effectively enlarge the accessible ECSA and favors better exposure and utilization of electrocatalytically active sites. iii) The self-supported 3D open architecture without any polymeric binders and conductive agents allows the easy penetration of electrolyte ions and mass transport and promotes the release of evolved gas bubbles, which is in favor of reaction kinetics and long-term electrochemical stability.

4. Conclusion

In summary, we have innovatively synthesized a hybrid nanocomposite catalyst consisting of ultrathin $Ni_{0.82}Co_{0.18}O$ nanosheets and coupled carbon on the surface of nickel foam ($Ni_{0.82}Co_{0.18}O@C/NF$) through a facile and low-cost immersion-adsorption-pyrolysis strategy. The hybrid $Ni_{0.82}Co_{0.18}O@C/NF$ can serve as a highly efficient bifunctional electrocatalyst for both HER and OER in alkaline media. The overpotentials to deliver 10 mA cm^{-2} for HER and 50 mA cm^{-2} for OER are merely 62 and 320 mV. Remarkably, it enables an overall water splitting device with a current density of 10 mA cm^{-2} at an ultralow cell voltage of 1.42 V, which is lower than most reported bifunctional catalysts and maintains its activity for more than 20 h. Considering the developed strategy is convenient and easily scalable, the highly efficient $Ni_{0.82}Co_{0.18}O@C/NF$ catalyst with low-cost and earth abundance would hold the promise for practical water-splitting devices.

Appendix A. Supplementary data

Supplementary material related to this article can be found, in the online version, at doi:https://doi.org/10.1016/j.apcatb.2019.04.021.

References

[1] Z.W. Seh, J. Kibsgaard, C.F. Dickens, I. Chorkendorff, J.K. Nørskov, T.F. Jaramillo, Combining theory and experiment in electrocatalysis: insights into materials design, Science 335 (2017) 146.

[2] Y.F. Liu, H.G. Pan, Y.J. Yue, X.F. Wu, N. Chen, Y.Q. Lei, Cycling durability and degradation behavior of La–Mg–Ni–Co-type metal hydride electrodes, J. Alloys. Compd. 395 (2005) 291–299.

[3] Y. Lin, M.X. Gao, D. Zhu, Y.F. Liu, H.G. Pan, Effects of carbon coating and iron phosphides on the electrochemical properties of LiFePO$_4$/C, J. Power Sources 184 (2008) 444–448.

[4] Y.Q. Yang, W.B. Zhang, Y.L. Xiao, Z.P. Shi, X.M. Cao, Y. Tang, Q.S. Gao, CoNiSe$_2$ heteronanorods decorated with layered-double-hydroxides for efficient hydrogen evolution, Appl. Catal. B: Environ. 242 (2019) 132–139.

[5] R.B. Wu, X.K. Qian, K. Zhou, J. Wei, J. Lou, P.M. Ajayan, Porous spinel Zn$_x$Co$_{3-x}$O$_4$ hollow polyhedra templated for high-rate lithium-ion batteries, ACS Nano 8 (2014) 6297–6303.

[6] Y.F. Liu, K. Zhong, K. Luo, M.X. Gao, H.G. Pan, Q.D. Wang, Size-dependent kinetic enhancement in hydrogen absorption and desorption of the Li-Mg-N-H system, J. Am. Chem. Soc. 131 (2009) 1862–1870.

[7] H.G. Pan, Y.F. Liu, M.X. Gao, Y.Q. Lei, Q.D. Wang, A study of the structural and electrochemical properties of La$_{0.7}$Mg$_{0.3}$(Ni$_{0.85}$Co$_{0.15}$)x (x=2.5~5.0) hydrogen storage electrode alloys, J. Electrochem. Soc. 150 (2003) A565–A570.

[8] Y.P. Pang, Y.F. Liu, M.X. Gao, L.Z. Ouyang, J.W. Liu, H. Wang, M. Zhu, H.G. Pan, A mechanical-force-driven physical vapour deposition approach to fabricating complex hydride nanostructures, Nat. Commun. 5 (2014) 1–8.

[9] H.G. Pan, Y.F. Liu, M.X. Gao, Y.F. Zhu, Y.Q. Lei, Q.D. Wang, An investigation on the structural and electrochemical properties of La$_{0.7}$Mg$_{0.3}$(Ni$_{0.85}$Co$_{0.15}$)x (x=3.15~3.80) hydrogen storage electrode alloys, J. Alloys. Compd. 351 (2003) 228–234.

[10] S.M. Zhang, H.T. Gu, H.G. Pan, S.H. Yang, W.B. Du, X. Li, M.X. Gao, Y.F. Liu, M. Zhu, L.Z. Ouyang, A novel strategy to suppress capacity and voltage fading of Li- and Mn-rich layered oxide cathode material for lithium-ion batteries, Adv. Energy Mater. 7 (2017) 1601066.

[11] Y.F. Liu, H.G. Pan, M.X. Gao, Q.D. Wang, Advanced hydrogen storage alloys for Ni/MH rechargeable batteries, J. Mater. Chem. 21 (2011) 4743–4755.

[12] I. Roger, M.A. Shipman, M.D. Symes, Earth-abundant catalysts for electrochemical and photoelectrochemical water splitting, Int. Rev. Chem. Eng. 1 (2017) 0003.

[13] Z.L. Chen, Y. Ha, Y. Liu, H.Y. Wang, H.Y. Yang, X.B. Xu, Y.J. Li, R.B. Wu, In situ formation of cobalt nitrides/graphitic carbon composites as efficient bifunctional electrocatalysts for overall water splitting, ACS Appl. Mater. Interfaces 10 (2018) 7134–7144.

[14] S. Dutta, A. Indra, Y. Feng, H. Hanc, T. Song, Promoting electrocatalytic overall water splitting with nanohybrid of transition metal nitride-oxynitride, Appl. Catal. B: Environ. 241 (2019) 521–527.

[15] Z.L. Chen, H.B. Xu, Y. Ha, X.Y. Li, M. Liu, R.B. Wu, Two-dimensional dual carbon-coupled defective nickel quantum dots towards highly efficient overall water splitting, Appl. Catal. B: Environ. 250 (2019) 213–223.

[16] H. Li, X.L. Zhao, H.L. Liu, S. Chen, X.F. Yang, C.X. Lv, H.W. Zhang, X.L. She, D.J. Yang, Sub-1.5 nm ultrathin CoP nanosheet aerogel: efficient electrocatalyst for hydrogen evolution reaction at all pH values, Small 14 (2018) 1802824.

[17] X. Wang, L.Z. Zhuang, T.W. He, Y. Jia, L.Z. Zhang, X.C. Yan, M.R. Gao, A.J. Du, Z.H. Zhu, X.D. Yao, S.H. Yu, Grafting cobalt diselenide on defective graphene for enhanced oxygen evolution reaction, iScience 7 (2018) 145–153.

[18] R.B. Wu, D.P. Wang, K. Zhou, N. Srikanth, J. Wei, Z. Chen, Porous cobalt phosphide/graphitic carbon polyhedral hybrid composites for efficient oxygen evolution reactions, J. Mater. Chem. A 4 (2016) 13742–13745.

[19] Z.L. Chen, R.B. Wu, Y. Liu, Y. Ha, Y.H. Guo, D.L. Sun, M. Liu, F. Fang, Ultrafine Co nanoparticles encapsulated in carbon-nanotubes-grafted graphene sheets as advanced electrocatalysts for the hydrogen evolution reaction, Adv. Mater. 30 (2018) 201802011.

[20] Z.L. Chen, M. Liu, R.B. Wu, Strongly coupling of Co$_9$S$_8$/Zn-Co-S heterostructures rooted in carbon nanocages towards efficient oxygen evolution reaction, J. Catal. 361 (2018) 322–330.

[21] Z.L. Chen, R.B. Wu, M. Liu, Y. Liu, S.Y. Xu, Y. Ha, Y.H. Guo, X.B. Yu, D.L. Sun, F. Fang, Tunable electronic coupling of cobalt sulfide/carbon composites for optimizing oxygen evolution reaction activity, J. Mater. Chem. A 6 (2018) 10304–10312.

[22] D.J. Yang, L.J. Zhang, X.C. Yan, X.D. Yao, Recent progress in oxygen electro-catalysts for zinc-air batteries, Small Methods 1 (2017) 1700209.

[23] X. Wang, L.Z. Zhuang, Y. Jia, H.L. Liu, X.C. Yan, L.Z. Zhang, D.J. Yang, Z.H. Zhu, X.D. Yao, Plasma-triggered synergy of exfoliation, phase transformation, and surface engineering in cobalt diselenide for enhanced water oxidation, Angew. Chem. Int. Ed. 57 (2018) 16421–16425.

[24] J. Staszak-Jirkovsky, C.D. Malliakas, P.P. Lopes, N. Danilovic, S.S. Kota, K.C. Chang, B. Genorio, D. Strmcnik, V.R. Stamenkovic, M.G. Kanatzidis, N.M. Markovic, Design of active and stable Co-Mo-S$_x$ chalcogels as pH-universal catalysts for the hydrogen evolution reaction, Nat. Mater. 15 (2016) 197–203.

[25] Z.L. Chen, Y. Ha, Y.X. Jia, X.X. Yan, M. Chen, M. Liu, R.B. Wu, Oriented transformation of Co-LDH into 2D/3D ZIF-67 to achieve Co-N-C hybrids for efficient overall water splitting, Adv. Energy Mater. 9 (2019) 1803918.

[26] M. Tavakkoli, T. Kallio, O. Reynaud, A.G. Nasibulin, C. Johans, J. Sainio, H. Jiang, E.I. Kauppinen, K. Laasonen, Single-shell carbon-encapsulated iron nanoparticles: synthesis and high electrocatalytic activity for hydrogen evolution reaction, Angew. Chem. Int. Ed. 54 (2015) 4535–4538.

[27] E.J. Popczun, C.G. Read, C.W. Roske, N.S. Lewis, R.E. Schaak, Highly active electrocatalysis of the hydrogen evolution reaction by cobalt phosphide nanoparticles, Angew. Chem. Int. Ed. 53 (2014) 5427–5430.

[28] E.L. Hu, J.Q. Ning, D. Zhao, C.Y. Xu, Y.Y. Lin, Y.J. Zhong, Z.Y. Zhang, Y.J. Wang, Y. Hu, A room-temperature postsynthetic ligand exchange strategy to construct mesoporous Fe-doped CoP hollow triangle plate arrays for efficient electrocatalytic water splitting, Small 14 (2018) 1704233.

[29] Q.C. Xu, H. Jiang, H.X. Zhang, Y.J. Hu, C.Z. Li, Heterogeneous interface engineered atomic configuration on ultrathin Ni(OH)$_2$/Ni$_3$S$_2$ nanoforests for efficient water splitting, Appl. Catal. B: Environ. 242 (2019) 60–66.

[30] A. Grimaud, O. Diaz-Morales, B.H. Han, W.T. Hong, Y.L. Lee, L. Giordano, K.A. Stoerzinger, M.T.M. Koper, Y. Shao-Horn, Activating lattice oxygen redox reactions in metal oxides to catalyse oxygen evolution, Nat. Chem. 9 (2017) 457–465.

[31] Y. Ha, L.X. Shi, Z.L. Chen, R.B. Wu, Phase-transited lysozyme-driven formation of self-supported Co$_3$O$_4$@C nanomeshes for overall water splitting, Adv. Sci. 6 (2019) 1900272.

[32] T.Y. Ma, S. Dai, M. Jaroniec, S.Z. Qiao, Metal–organic framework derived hybrid Co$_3$O$_4$-carbon porous nanowire arrays as reversible oxygen evolution electrodes, J. Am. Chem. Soc. 136 (2014) 13925–13931.

[33] A. Aijaz, J. Masa, C. Rösler, W. Xia, P. Weide, A.J.R. Botz, R.A. Fischer, W. Schuhmann, M. Muhler, Co@Co$_3$O$_4$ encapsulated in carbon nanotube-grafted nitrogen-doped carbon polyhedra as an advanced bifunctional oxygen electrode, Angew. Chem. Int. Ed. 55 (2016) 4087–4091.

[34] J. Zhang, Y. Wang, C. Zhang, H. Gao, L.F. Lv, L.L. Han, Z.H. Zhang, Self-Supported porous NiSe$_2$ nanowrinkles as efficient bifunctional electrocatalysts for overall water splitting, ACS Sustain. Chem. Eng. 6 (2018) 2231–2239.

[35] J.S. Luo, J.H. Im, M.T. Mayer, M. Schreier, M.K. Nazeeruddin, N.G. Park, S.D. Tilley, H.J. Fan, M. Grätzel, Water photolysis at 12.3% efficiency via perovskite photovoltaics and earth-abundant catalysts, Science 345 (2014) 1593–1596.

[36] Y. Jia, L.Z. Zhang, G.P. Gao, H. Chen, B. Wang, J.Z. Zhou, M.T. Soo, M. Hong, X.C. Yan, G.R. Qian, J. Zou, A.J. Du, X.D. Yao, Graphene as a bifunctional electrocatalyst for overall water splitting, Adv. Mater. 29 (2017) 1700017.

[37] E.L. Hu, Y.F. Feng, J.W. Nai, D. Zhao, Y. Hu, X.W. Lou, Construction of hierarchical Ni–Co–P hollow nanobricks with oriented nanosheets for efficient overall water splitting, Energy Environ. Sci. 11 (2018) 872–880.

[38] Y.F. Feng, C.Y. Xu, E.L. Hu, B.B. Xia, J.Q. Ning, C.C. Zheng, Y.J. Zhong, Z.Y. Zhang, Y. Hu, Construction of hierarchical FeP/Ni$_2$P hollow nanospindles for efficient oxygen evolution, J. Mater. Chem. A 6 (2018) 14103–14111.

[39] P.Z. Chen, T.P. Zhou, M.X. Zhang, Y. Tong, C. Zhong, N. Zhang, L.D. Zhang, C.Z. Wu, Y. Xie, 3D nitrogen-anion-decorated nickel sulfides for highly efficient overall water splitting, Adv. Mater. 29 (2017) 1701584.

[40] Y. Gu, S. Chen, J. Ren, Y.A. Jia, C.M. Chen, S. Komarneni, D.J. Yang, X.D. Yao, Electronic structure tuning in Ni$_3$FeN/r-GO aerogel toward bifunctional electrocatalyst for overall water splitting, ACS Nano 12 (2018) 245–253.

[41] J. Zhang, T. Wang, D. Pohl, B. Rellinghaus, R. Dong, S.H. Liu, X.D. Zhang, X.L. Feng, Interface engineering of MoS$_2$/Ni$_3$S$_2$ heterostructures for highly enhanced electrochemical overall-water-splitting activity, Angew. Chem. Int. Ed. 55 (2016) 6702–6707.

[42] G.A. El-Nagar, M.A. Hassanc, A. Fetyan, M.K. Kayarkatte, I. Lauermannd, C. Roth, A promising N-doped carbon-metal oxide hybrid electrocatalyst derived from Crustacean's shells: oxygen reduction and oxygen evolution, Appl. Catal. B: Environ. 214 (2017) 137–147.

[43] C.Q. Dong, T.Y. Kou, H. Gao, Z.Q. Peng, Z.H. Zhang, Eutectic-derived mesoporous Ni-Fe-O nanowire network catalyzing oxygen evolution and overall water splitting, Adv. Energy Mater. 8 (2018) 1701347.

[44] H.J. Zhang, X.P. Li, A. Hähnel, V. Naumann, C. Lin, S. Azimi, S.L. Schweizer, A.W. Maijenburg, R.B. Wehrspohn, Bifunctional heterostructure assembly of NiFe LDH nanosheets on NiCoP nanowires for highly efficient and stable overall water splitting, Adv. Funct. Mater. 28 (2018) 1706847.

[45] C.L. Hu, L. Zhang, Z.J. Zhao, A. Li, X.X. Chang, J.L. Gong, Synergism of geometric construction and electronic regulation: 3D Se-(NiCo)S$_x$/(OH)$_x$ nanosheets for highly efficient overall water splitting, Adv. Mater. 30 (2018) 1705538.

[46] Z.C. Wang, H.L. Liu, R.X. Ge, X. Ren, J. Ren, D.J. Yang, L.X. Zhang, X.P. Sun, Phosphorus-doped Co$_3$O$_4$ nanowire array: a highly efficient bifunctional electrocatalyst for overall water splitting, ACS Catal. 8 (2018) 2236–2241.

[47] Z. Li, W.H. Niu, L. Zhou, Y. Yang, Phosphorus and aluminum codoped porous NiO nanosheets as highly efficient electrocatalysts for overall water splitting, ACS Energy Lett. 3 (2018) 892–898.

[48] C.Y. Xu, Z. Lin, D. Zhao, Y.L. Sun, Y.J. Zhong, J.Q. Ning, C.C. Zheng, Z.Y. Zhang,

Y. Hu, Facile in situ fabrication of Co nanoparticles embedded in 3D N-enriched mesoporous carbon foam electrocatalyst with enhanced activity and stability toward oxygen reduction reaction, J. Mater. Sci. 54 (2019) 5412–5423.

[49] J.F. Xie, X.D. Zhang, H. Zhang, J.J. Zhang, S. Li, R.X. Wang, B.C. Pan, Y. Xie, Intralayered ostwald ripening to ultrathin nanomesh catalyst with robust oxygen-evolving performance, Adv. Mater. 29 (2017) 1604765.

[50] L. Trotochaud, S.L. Young, J.K. Ranney, S.W. Boettcher, Nickel-iron oxyhydroxide oxygen-evolution electrocatalysts: the role of intentional and incidental iron incorporation, J. Am. Chem. Soc. 136 (2014) 6744–6753.

[51] H.J. Liu, Q. He, H.L. Jiang, Y.X. Lin, Y.K. Zhang, M. Habib, S.M. Chen, L. Song, Electronic structure reconfiguration toward pyrite NiS_2 via engineered heteroatom defect boosting overall water splitting, ACS Nano 11 (2017) 11574–11583.

[52] W.J. Hao, R.B. Wu, R.Q. Zhang, Y. Ha, Z.L. Chen, L.C. Wang, Y.J. Yang, X.H. Ma, D.L. Sun, F. Fang, Y.H. Guo, Electroless plating of highly efficient bifunctional boride-based electrodes toward practical overall water splitting, Adv. Energy Mater. 8 (2018) 1801372.

[53] Y.Y. Liang, Y.G. Li, H.L. Wang, J.G. Zhou, J. Wang, T. Regier, H.J. Dai, Co_3O_4 nanocrystals on graphene as a synergistic catalyst for oxygen reduction reaction, Nat. Mater. 10 (2011) 780–786.

[54] S.C. Huang, Y.Y. Meng, S.M. He, A. Goswami, Q.L. Wu, J.H. Li, S.F. Tong, T. Asefa, M.M. Wu, N-, O-, and S-tridoped carbon-encapsulated Co_9S_8 nanomaterials: efficient bifunctional electrocatalysts for overall water splitting, Adv. Funct. Mater. 27 (2017) 1606585.

[55] Q.Y. Wu, P. Diao, J. Sun, D. Xu, T. Jin, M. Xiang, Draining the photoinduced electrons away from an anode: the preparation of $Ag/Ag3PO_4$ composite nanoplate photoanodes for highly efficient water splitting, J. Mater. Chem. A 3 (2015) 18991–18999.

[56] G. Nagaraju, S.C. Sekhar, L.K. Bharat, J.S. Yu, Wearable fabrics with self-branched bimetallic layered double hydroxide coaxial nanostructures for hybrid supercapacitors, ACS Nano 11 (2017) 10860–10874.

[57] A. Sivanantham, S. Shanmugam, Nickel selenide supported on nickel foam as an efficient and durable non-precious electrocatalyst for the alkaline water electrolysis, Appl. Catal. B: Environ. 203 (2017) 485–493.

[58] X.D. Yan, K.X. Li, L. Lyu, F. Song, J. He, D.M. Niu, L. Liu, X.L. Hu, X.B. Chen, From

water oxidation to reduction: transformation from $Ni_xCo_{3-x}O_4$ nanowires to $NiCo/NiCoO_x$ heterostructures, ACS Appl. Mater. Interfaces 8 (2016) 3208–3214.

[59] C. Lamiel, V.H. Nguyen, I. Hussain, J.J. Shim, Enhancement of electrochemical performance of nickel cobalt layered double hydroxide@ nickel foam with potassium ferricyanide auxiliary electrolyte, Energy 140 (2017) 901–911.

[60] J. Liu, D. Zhu, T. Ling, A. Vasileff, S.Z. Qiao, $S\text{-}NiFe_2O_4$ ultra-small nanoparticle built nanosheets for efficient water splitting in alkaline and neutral pH, Nano Energy 40 (2017) 264.

[61] Z.L. Chen, R.B. Wu, M. Liu, H. Wang, Y. Song, F. Fang, X.B. Yu, D.L. Sun, General synthesis of dual carbon-confined metal sulfides quantum dots towards high-performance anodes for sodium-ion batteries, Adv. Funct. Mater. 9 (2017) 1702046.

[62] L. Yan, Y.L. Sun, E.L. Hu, J.Q. Ning, Y.J. Zhong, Z.Y. Zhang, Y. Hu, Facile in-situ growth of Ni_2P/Fe_2P nanohybrids on Ni foam for highly efficient urea electrolysis, J. Colloid Interface Sci. 541 (2019) 279–286.

[63] H.H. Liu, K.F. Tian, J.Q. Ning, Y.J. Zhong, Z.Y. Zhang, Y. Hu, One-step solvothermal formation of Pt nanoparticles decorated Pt^{2+}-doped $\alpha\text{-}Fe_2O_3$ nanoplates with enhanced photocatalytic O_2 evolution, ACS Catal. 9 (2019) 1211–1219.

[64] Z.C. Wu, X. Wang, J.S. Huang, F. Gao, A Co-doped Ni–Fe mixed oxide mesoporous nanosheet array with low overpotential and high stability towards overall water splitting, J. Mater. Chem. A 6 (2018) 167–178.

[65] Y. Zhang, Y.L. Ma, Y.Y. Chen, L. Zhao, L.B. Huang, H. Luo, W.J. Jiang, X. Zhang, S. Niu, D.J. Gao, J. Bi, G.Y. Fan, J.S. Hu, Encased copper boosts the electrocatalytic activity of N-doped carbon nanotubes for hydrogen evolution, ACS Appl. Mater. Interfaces 9 (2017) 36857–36864.

[66] B.W. Zhang, Y.H. Lui, H.W. Ni, S. Hu, Bimetallic $(Fe_xNi_{1-x})_2P$ nanoarrays as exceptionally efficient electrocatalysts for oxygen evolution in alkaline and neutral media, Nano Energy 38 (2017) 553–560.

[67] Y. Pan, H.J. Ren, H.W. Du, F.Y. Cao, Y.F. Jiang, H.J. Du, D.W. Chu, Active site engineering by surface sulfurization for a highly efficient oxygen evolution reaction: a case study of Co_3O_4 electrocatalysts, J. Mater. Chem. A 6 (2018) 22497–22502.

[68] L. Zhang, P.F. Liu, Y.H. Li, C.W. Wang, M.Y. Zu, H.Q. Fu, X.H. Yang, H.G. Yang, Accelerating neutral hydrogen evolution with tungsten modulated amorphous metal hydroxides, ACS Catal. 8 (2018) 5200–5205.